


Article

Hetero-Optomechanical Crystal Zipper Cavity for Multimode Optomechanics

Ning Wu^{1,2}, Kaiyu Cui^{1,2,*}, Xue Feng^{1,2} , Fang Liu^{1,2}, Wei Zhang^{1,2,3} and Yidong Huang^{1,2,3}

¹ Department of Electronic Engineering, Tsinghua University, Beijing 100084, China; wun18@mails.tsinghua.edu.cn (N.W.); x-feng@tsinghua.edu.cn (X.F.); liu_fang@mail.tsinghua.edu.cn (F.L.); zwei@tsinghua.edu.cn (W.Z.); yidonghuang@tsinghua.edu.cn (Y.H.)

² Beijing National Research Center for Information Science and Technology (BNRist), Tsinghua University, Beijing 100084, China

³ Beijing Academy of Quantum Information Sciences, Beijing 100193, China

* Correspondence: kaiyucui@tsinghua.edu.cn

Abstract: Multimode optomechanics exhibiting several intriguing phenomena, such as coherent wavelength conversion, optomechanical synchronization, and mechanical entanglements, has garnered considerable research interest for realizing a new generation of information processing devices and exploring macroscopic quantum effect. In this study, we proposed and designed a hetero-optomechanical crystal (OMC) zipper cavity comprising double OMC nanobeams as a versatile platform for multimode optomechanics. Herein, the heterostructure and breathing modes with high mechanical frequency ensured the operation of the zipper cavity at the deep-sideband-resolved regime and the mechanical coherence. Consequently, the mechanical breathing mode at 5.741 GHz and optical odd mode with an intrinsic optical Q factor of 3.93×10^5 were experimentally demonstrated with an optomechanical coupling rate $g_0 = 0.73$ MHz between them, which is comparable to state-of-the-art properties of the reported OMC. In addition, the hetero-zipper cavity structure exhibited adequate degrees of freedom for designing multiple mechanical and optical modes. Thus, the proposed cavity will provide a playground for studying multimode optomechanics in both the classical and quantum regimes.

Keywords: hetero-optomechanical crystals; zipper cavity; multimode optomechanics



Citation: Wu, N.; Cui, K.; Feng, X.; Liu, F.; Zhang, W.; Huang, Y. Hetero-Optomechanical Crystal Zipper Cavity for Multimode Optomechanics. *Photonics* **2022**, *9*, 78. <https://doi.org/10.3390/photronics9020078>

Received: 31 December 2021

Accepted: 27 January 2022

Published: 29 January 2022

Publisher's Note: MDPI stays neutral with regard to jurisdictional claims in published maps and institutional affiliations.



Copyright: © 2022 by the authors. Licensee MDPI, Basel, Switzerland. This article is an open access article distributed under the terms and conditions of the Creative Commons Attribution (CC BY) license (<https://creativecommons.org/licenses/by/4.0/>).

1. Introduction

Cavity optomechanics focuses on the interaction between mechanical oscillators and light in optical cavities, and is a promising architecture for the research of macroscopic quantum effect and realizing a new generation of information processing devices [1,2]. Recently, significant progress has been achieved in cooling the mechanical oscillator into the quantum ground state [3,4], phenomena of optomechanical induced transparency [5,6], strong optomechanical coupling effect [7,8], and optomechanical sensing [9–12] to explore the interaction between single optical cavity mode and single mechanical mode.

Further, this optomechanical interaction has been investigated in a more general form containing multiple mechanical and optical modes. The multimode optomechanical model causes several intriguing phenomena beyond the description of the “minimum model”, namely, the coherent wavelength conversion [13,14], optomechanical synchronization [15,16], the topological energy transfer [17,18], the nonreciprocal dynamics [19], and mechanical entanglement [20]. Despite these advancements, multimode optomechanical platforms including microdisk cavities [21], silicon nitride membranes [22], plasmonic nanoresonators [23–25], and semiconductor nanowires [26] still focus on the mechanical modes with low frequency that limit the coherence of the optomechanical system. It is noticed that the confinement of the optical and mechanical modes in a wavelength scale via photonic and phononic quasiperiodic structures enables optomechanical crystals

(OMCs) to provide high-frequency mechanical modes at the GHz-scale, long decoherence time, and strong optomechanical coupling rate [27]. However, conventional architectures based on a single nanobeam OMC are not appropriate candidates for studying multimode optomechanics as they lack the flexibility to design the properties of multiple modes.

In this study, we focused on the GHz-scale multiple mechanical modes and proposed the hetero-OMC zipper cavity as a versatile platform. The zipper cavity comprised double nanobeam OMC cavities with heterostructures [28], which are advantageous for realizing high mechanical frequency and maintaining the coherence of mechanical modes simultaneously. Here, the optomechanical coupling rate and the optical quality factor were optimized for designing the zipper cavity. Subsequently, both the optical and mechanical properties of the fabricated device which operates at the deep-sideband-resolved regime were characterized using a blue detuned pump light. The experimental results show that a mechanical breathing mode at 5.741 GHz and an optical odd mode with the intrinsic optical Q of 3.93×10^5 were coupled to each other at a high optomechanical coupling rate g_0 of 0.73 MHz. Based on the design flexibility of the hetero-OMC zipper cavity and its high performance, the proposed cavity offered tremendous possibilities as a versatile platform for studying multimode optomechanics in both the classical and quantum regimes.

2. Methods

2.1. Design of Hetero-OMC Zipper Cavity

The hetero-OMC zipper cavity is presented in Figure 1a, comprising two identical OMC nanobeams which can be divided into OMC unit cells, as depicted in Figure 1b. Accordingly, a heteroregion and a defect region can be characterized. The P-I and P-II quasiperiodic regions with different constant structure parameters and bandgaps constitute the heterostructure. They act as the photonic mirror and the phononic mirror, respectively [10,28]. For the defect region, the radius of the air hole r_i and the distance d_i between the adjacent holes gradually increase from the center toward the exterior, and the optical and mechanical modes with discrete resonant frequencies were formed in this effective potential well.

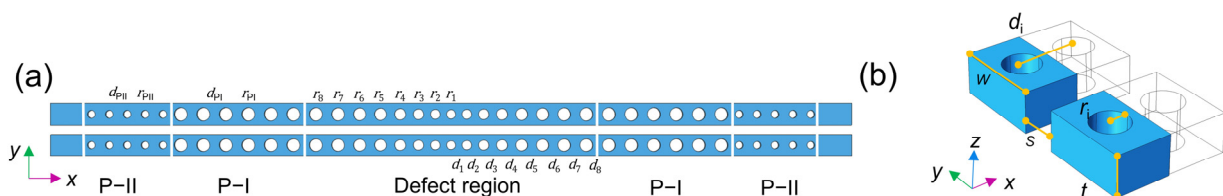


Figure 1. (a) Top view of the hetero-optomechanical crystal (OMC) zipper cavity. (b) Structural parameters in OMC unit cell.

Among these resonant modes, the optical modes were symmetrically distributed on the two nanobeams of the zipper cavity, which can be further classified into two types: optical even modes and odd modes. As illustrated in Figure 2a, the electric fields tend to concentrate in the zipper gap for the even modes and are located farther from the zipper gap for the odd modes. These even and odd modes result from the coupling between the degenerate optical modes in each nanobeam. On the contrary, there is no direct mechanical coupling between the mechanical modes in two nanobeams because the two nanobeams of the zipper cavity are independent of each other.

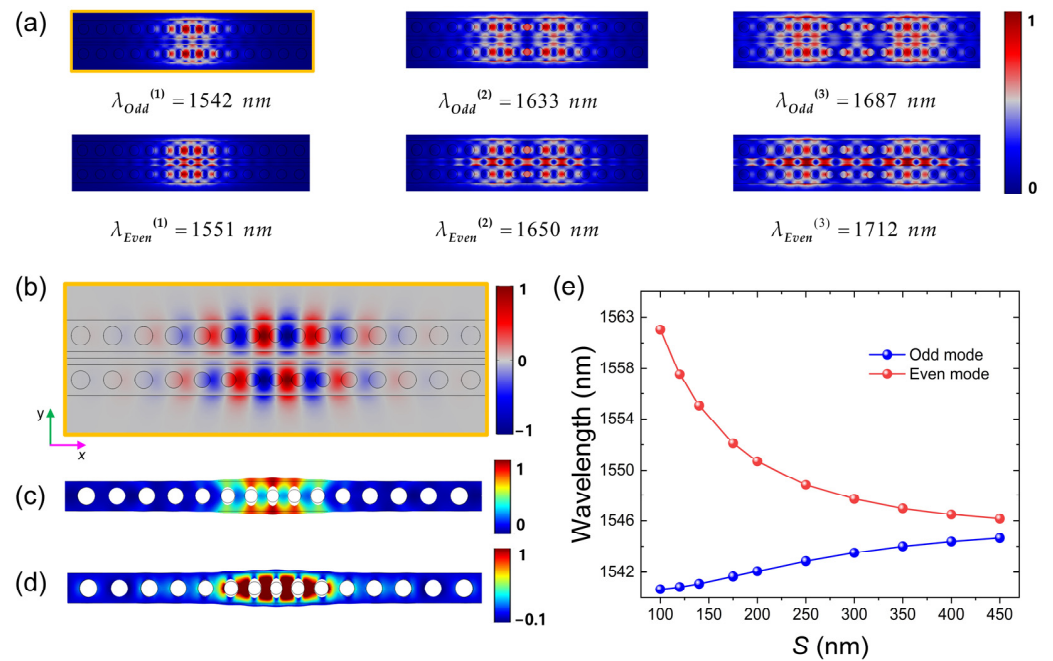


Figure 2. (a) Normalized amplitude of electric field $|E|$ for various orders of even and odd optical modes. (b) Normalized electric field component E_y of first-order optical odd mode. (c) Normalized amplitude of displacement field of 5.635 GHz mechanical breathing mode in an arm of zipper cavity. (d) Strain tensor component S_{yy} for mechanical breathing mode. (e) Optical resonant wavelengths of the first-order even and odd mode versus gap length s . (a–e) Both the mechanical modes and the optical modes are simulated via the finite element method.

Notably, as the two nanobeams of the zipper cavity are independent, the zipper cavity structure provides the flexibility for designing multiple optical and mechanical modes. In this architecture, the near-degenerate optical and mechanical modes, which are essential for multimode optomechanics, are easy to be obtained. In addition, in combination with the heterostructure, this structure gives the freedom for manipulating the loss of the mechanical and optical modes independently [10,28]. Meanwhile, the optomechanical interaction between the optical and mechanical modes, which is determined by the profile of the optical and mechanical modes, can also be adjusted effectively in the zipper cavity with a suitable geometrical design of the defect region.

For this zipper cavity, the optomechanical interaction strength can be primarily characterized using the optomechanical coupling rate g_0 , which was defined as the resonant frequency shift of an optical mode resulting from the zero-point motion of a mechanical mode in one of the nanobeams [1]. Thus, the strong optomechanical coupling rate g_0 enables the investigation and utilization of novel optomechanical effects. As an OMC, the optomechanical coupling rate of the zipper cavity is contributed by the photoelastic effect and moving boundary effect [28–30], where the mechanical motion altered the refractive index and geometry of the zipper cavity, respectively. The optical quality factor constitutes another vital parameter in the optomechanical coupling process. High optical quality factor ensures the long lifetime of cavity photons and improves the ability to control mechanical modes via enhancing one of the photon–phonon coupling processes (stokes or anti-stokes process) in light scattering [1,2]. Therefore, in this study, we designed the hetero-OMC zipper cavity with both high optomechanical coupling rate g_0 and high optical quality factor Q .

Specifically, the overlapping of the optical and mechanical modes in the defect region should be enhanced to attain a high g_0 . Meanwhile, the high-quality factor of the optical modes requires the suppression of the mode-leaking via the waveguide as well as the mode-scattering into free space. Accordingly, these targets are fulfilled by designing the

geometric parameters of the OMC unit cell illustrated in Figure 1b. In the current design, the radius of the air hole r_i and the distance d_i between the adjacent holes were the design variables following Equation (1), whereas the thickness of the device layer ($t = 220$ nm) and the gap between two nanobeams ($s = 200$ nm) were fixed as constants.

$$\left\{ \begin{array}{l} r_i = r_{PI} + (r_1 - r_{PI}) \times \frac{e^{-(\frac{i}{N_r})^2} - e^{-(\frac{9}{N_r})^2}}{e^{-(\frac{1}{N_r})^2} - e^{-(\frac{9}{N_r})^2}} \quad (1 \leq i \leq 8) \\ r_i = r_{PI} \quad (9 \leq i \leq 14) \qquad \qquad \qquad r_i = r_{PII} \quad (15 \leq i \leq 19) \\ d_i = \left(l_{PI} + (l_1 - l_{PI}) \times \frac{e^{-(\frac{i}{N_d})^2} - e^{-(\frac{9}{N_d})^2}}{e^{-(\frac{1}{N_d})^2} - e^{-(\frac{9}{N_d})^2}} \right) \times (r_i + r_{i+1}) \quad (1 \leq i \leq 8) \\ d_i = d_{PI} \quad (9 \leq i \leq 14) \qquad \qquad \qquad d_i = d_{PII} \quad (15 \leq i \leq 18) \end{array} \right. \quad (1)$$

In Equation (1), r_i and d_i of the defect region were determined using six parameters ($N_r, N_d, r_1, r_{PI}, l_1, l_{PI}$). The Gaussian function controlled by parameters (N_r, N_d) was used to ensure adequate freedom for designing the structure and parameters (l_1, l_{PI}) was used to determine the ratio between d_i and r_i . In addition to r_i and d_i , the width of the nanobeam W was varied for the geometry design. Therefore, we could alter seven parameters ($N_r, N_d, r_1, r_{PI}, l_1, l_{PI}, W$) in total to optimize g_0 and Q . Here the properties of optical modes and mechanical modes were simulated based on the finite element method. In addition, the overlap integral between the optical modes and mechanical modes were calculated to acquire the optomechanical coupling rate g_0 [30]. Subsequently, we used the results of g_0 and Q as the optimization target to design the structure parameters with the simulated annealing algorithm [31]. In the current design, the structure parameters $N_r, N_d, r_1, r_{PI}, l_1, l_{PI}$, and W were optimized as 4.56, 4.79, 99 nm, 143 nm, 1.68, 1.73, and 472 nm, respectively. Thereafter, the P-II region can be independently designed to inhibit the mechanical radiation loss, and the hole radius and distance were designed as $r_{PII} = 85$ nm and $d_{PII} = 391$ nm.

For the proposed zipper cavity, the first-order optical modes and mechanical breathing mode exhibited excellent performance after the optimization process, and thus, were considered as the target modes. The high-order optical modes with the extended mode profile were not considered, because their resonant wavelengths were proximate to the edge of the bandgap of the unit cell in the P-I region, which considerably degraded their optical quality factors. For the first-order optical odd mode, it resonated at $\lambda_{odd} = 1542$ nm with the corresponding quality factor at $Q_{odd} = 5 \times 10^5$ in our simulation. The electric field of the first-order optical odd mode was primarily distributed at the center of the defect region, and the dominant component E_y is presented in Figure 2b, wherein the electric fields in the adjacent unit cells were out-of-phase, because the wavenumber of the excitation modes in the unit cell of the cavity center was proximate to the X point and situated farther from the light line [28].

The mechanical breathing mode in one of the nanobeams with the intrinsic resonant frequency $\Omega_{mi} = 5.635$ GHz is presented in Figure 2c, and it can interact with the even or odd optical mode. As depicted in Figure 2d, the optomechanical coupling was further characterized based on the main component of the strain tensor S_{yy} for this mechanical breathing mode. The S_{yy} components were in-phase in the adjacent unit cells of the cavity center, which appropriately overlapped with the electric field E_y shown in Figure 2b. Therefore, the photoelastic effect strongly contributed toward the optomechanical coupling rate, considering its contribution $g_{pe} \propto \int p_{11} S_{yy} |E_y|^2 dV$ in this condition [28–30], where p_{11} denotes one of the photoelastic coefficients. Ultimately, the simulation results indicate that a strong optomechanical coupling rate $g = 0.65$ MHz was obtained in this design with a contribution of 0.5 MHz from the photoelastic effect and 0.15 MHz from the moving boundary effect.

After completing the cavity design, the influence of the zipper gap length s on the optical modes was discussed, as illustrated in Figure 2e. This is because the optical resonant frequencies and frequency splitting of the first-order optical modes for this zipper cavity

architecture can be effectively tuned by varying s . As can be observed from Figure 2e, the resonant wavelength increased (decreased) for the even (odd) mode for a decreasing s . This shift in the trend of wavelength can be explained as the moving boundary effect [28–30], as the dominant component E_y is focused in the gap for the even mode, whereas the opposite is true for the odd mode. Similarly, the wavelength shift was larger for the same amount of variation in s in case of a small s for the even mode, because a stronger electric field E_y exists in the middle of the gap in case s is reduced further. This tunability of the optical resonant frequency might be available to realize a reconfigurable OMC device. For instance, the optomechanical-induced transparency (OMIT) phenomenon can be feasibly used for information processing and storage [32] at a wide frequency range with the introduction of microelectromechanical systems (MEMS)-driven scheme [33].

2.2. Fabrication and Measurements

Upon determining the parameters of the zipper cavity, this structure was fabricated on a silicon on insulator (SOI) chip. First, the designed pattern was defined on the electron beam photoresist coating present on the top of this SOI chip by using electron beam lithography (EBL). Thereafter, this pattern was transferred to the silicon layer using inductively coupled plasma (ICP) etching, and the photoresist was removed. Subsequently, the buried layer with a thickness of 3 μm was removed by the buffered hydrofluoric acid [34]. Lastly, the fabricated OMC zipper cavity is presented in Figure 3a, wherein the oblique view of the scanning electron microscopy (SEM) image indicated the suspension of the structure.

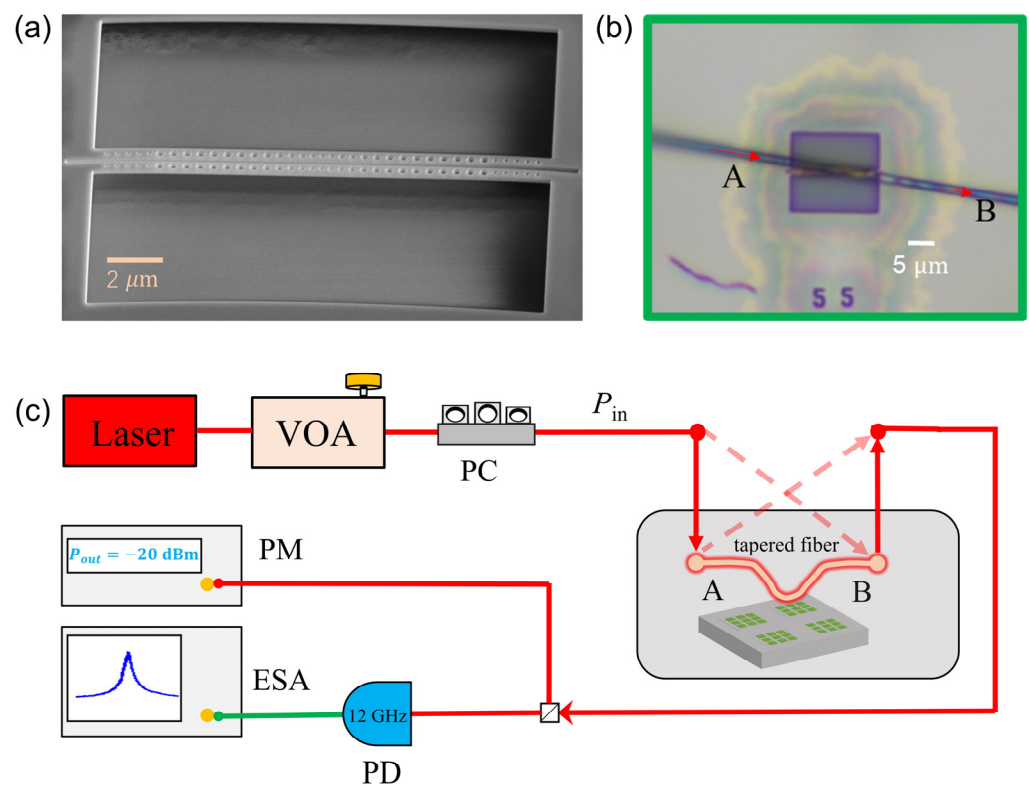


Figure 3. (a) Oblique view of scanning electron microscopy (SEM) image of a hetero-OMC zipper cavity. (b) Optical microscope image of a zipper cavity with a tapered fiber attached on top. (c) Schematic of experimental setup. VOA: variable optical attenuator; PC: polarization controller; PM: power meter; PD: photodetector; ESA: electric spectrum analyzer. Green and red lines represent path of electric signal and light path, respectively.

To experimentally characterize the fabricated OMC zipper cavity, the setup of the experiment is illustrated in Figure 3c. Concretely, a pump laser with frequency ω_L passes through the variable optical attenuator (VOA) and polarization controller (PC) to control

the power and polarization of pump light, respectively. Subsequently, as depicted in Figure 3b, the laser with power P_{in} at port A was transmitted into a tapered fiber with 1.5 μm diameter, which was attached on the OMC zipper cavity to excite the optical modes with a resonant frequency ω_{cav} . In this cavity, the information of the mechanical oscillation was mapped onto the optical signal owing to the optomechanical coupling. Ultimately, the optical signal output from port B was detected by the electric spectrum analyzer (ESA) to analyze the mechanical spectrum, whereas the power meter (PM) at the output port was used to monitor the optical power. In addition, the dashed line indicated an alternative light path in which port B is regarded as the input channel and port A is the output channel. This path is used for calibrating the intracavity photon number n_{cav} , as described in Section 3.

3. Results and Discussion

Based on the fabricated structure and the experimental setup discussed earlier, the normalized optical transmission spectra at low input power are represented in Figure 4a, where the first-order optical odd (even) mode resonated at 1548.9 nm (1555.6 nm), and they were consistent with the simulation results. In addition, a high intrinsic optical quality factor of $Q_i^{odd} = 3.9 \times 10^5$ ($Q_i^{even} = 3.7 \times 10^5$) was obtained for the odd (even) mode. Thus, this system operates in the deep-sideband-resolved regime, wherein the optical dissipation rate $k_{odd}/2\pi = 0.538$ GHz ($k_{even}/2\pi = 0.58$ GHz) is much smaller than the intrinsic mechanical resonant frequency $\Omega_{mi}/2\pi$ (~ 5.7 GHz) [35].

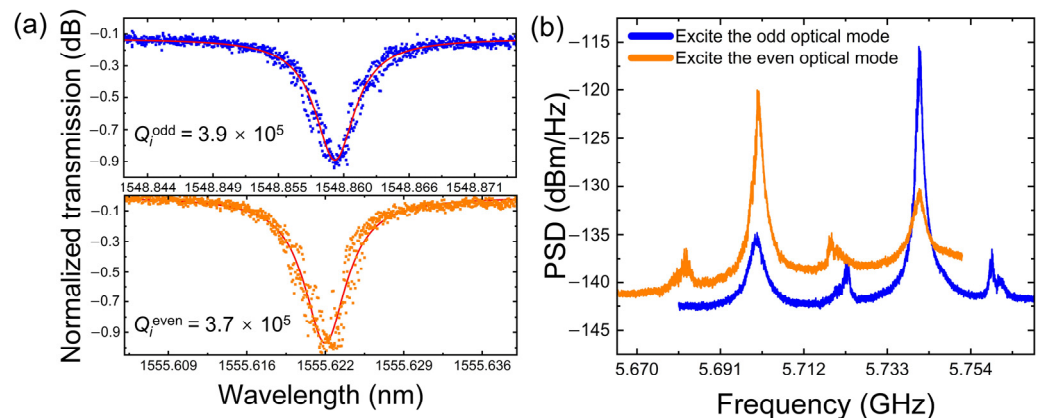


Figure 4. (a). Transmission spectra of first-order optical odd and even modes. (b). Power spectrum density (PSD) of mechanical spectrum analyzed by ESA for exciting odd and even optical modes, respectively.

Subsequently, the optical odd and even mode were separately excited to interact with the mechanical modes under identical input power P_{in} . The power spectrum density (PSD) of the electric signals carried the mechanical information and was detected by the ESA, as illustrated in Figure 4b. The peak of the spectra at the vicinity of 5.7 GHz and 5.74 GHz corresponded to the mechanical breathing modes in each arm of the zipper cavity. The PSD peak of the higher (lower) frequency mechanical mode was larger when exciting the odd (even) optical mode, and it indicated that the optical odd (even) mode tended to interact with the 5.74 (5.7) GHz mechanical mode. This was caused by the asymmetrical optical field distribution for two nanobeams of the fabricated zipper cavity that were not identical.

Further, the calibration of the intracavity photon number n_{cav} was essential prior to analyzing the influence of the pump light on the properties of mechanical modes. In this experiment, we used the thermo-optic effect to calibrate the optical loss in the two sections of the tapered fiber [3,36], which included the optical loss L_A from port A to the coupling region and the optical loss L_B from the coupling region to port B. As illustrated in Figure 5a, upon sweeping from the blue to the red side of the cavity resonance with high pump power, the optical resonant frequency initially shifted toward the long wavelength as the effective temperature of the cavity increased with the intracavity photon number n_{cav} . Accordingly,

the detuning $\Delta = \omega_L - \omega_{cav}$ and the optical transmission gradually varies. However, a further increase in the wavelength of the pump laser will shift the laser wavelength away from the cavity resonance, and consequently, decrease the intracavity photon number n_{cav} . Therefore, the effective temperature of the cavity will reduce and cause a blue shift of the cavity resonance. This positive feedback related to the bistable state [37] contributed toward the dramatic variation of the transmission and cavity detuning. In addition, as the pump power increases, the thermo-optic effect is enhanced and the bottom of the transmission spectrum shifts toward the long wavelength.

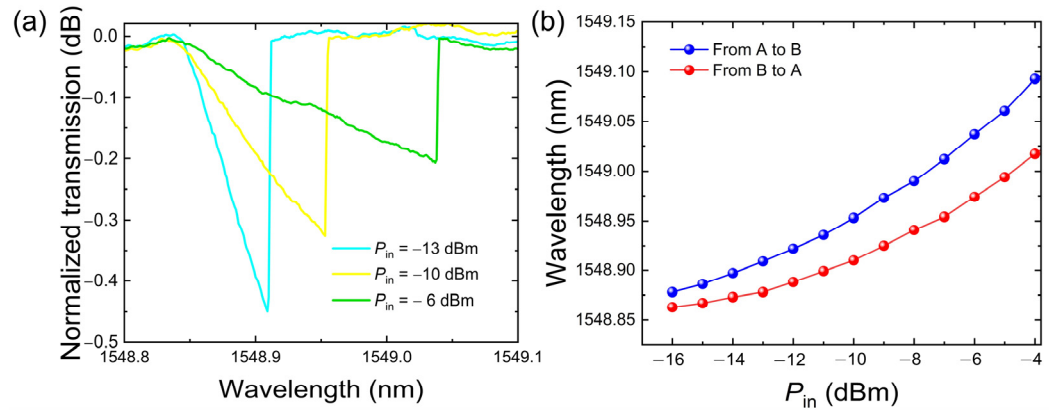


Figure 5. (a). Normalized optical transmission spectra swept from short to long wavelength under high input power P_{in} from port A to port B with $P_{in} = -13$ dBm, -10 dBm, and -6 dBm, respectively. (b). Wavelength at bottom of transmission spectra versus input laser power with blue (red) points representing experimental data in case A (B) is input port.

As the thermal optical effect is relevant to n_{cav} , the corresponding wavelength at the bottom of the transmission spectrum is distinct for a laser input from port A or port B when the loss L_A and L_B are not identical. Accordingly, the variation in the asymmetric frequency shift with the input power is presented in Figure 5b. For the same amount of frequency shift, the light power needed from port A and port B are different, and the difference of light power corresponds to the difference of loss $L_A - L_B$. As a result, the loss L_A and L_B can be obtained in case the total optical loss in the tapered fiber is known. In our measurement, L_A and L_B were 0.5 dB and 3.2 dB, respectively.

The PSD detected by the ESA was analyzed to characterize the mechanical properties, which can be expressed as $S_{PP}(\Omega) = H(\Delta)S_{\omega\omega}(\Omega)$ [38], where $H(\Delta)$ denotes the transduction function depending on the detuning Δ , and $S_{\omega\omega}$ represents the spectrum of the cavity resonance frequency fluctuations, expressed as:

$$S_{\omega\omega}(\Omega) = g_0^2 \frac{\gamma_i n_b}{(\Omega - \Omega_m)^2 + (\frac{\gamma}{2})^2} \tag{2}$$

where γ_i denotes the intrinsic dissipation rate of the mechanical mode and n_b represents the average phonon occupancy at frequency $\Omega/2\pi$. Consequently, the frequency fluctuations $S_{\omega\omega}$ can be fitted to obtain the experiment results of the mechanical linewidth $\gamma/2\pi$ and resonant frequency $\Omega_m/2\pi$. Theoretically, they can be expressed as Equation (3), where the mechanical frequency and linewidth were controlled using the blue detuned pump light via the optical spring effect and anti-damping effect, respectively [11].

$$\begin{aligned} \Omega_m &\approx \Omega_{mi} + g_0^2 n_{cav} \left(\frac{\Delta + \Omega_{mi}}{(\Delta + \Omega_{mi})^2 + (\frac{k}{2})^2} + \frac{\Delta - \Omega_{mi}}{(\Delta - \Omega_{mi})^2 + (\frac{k}{2})^2} \right) \\ \gamma &\approx \gamma_i + g_0^2 n_{cav} \left(\frac{k}{(\Delta + \Omega_{mi})^2 + (\frac{k}{2})^2} - \frac{k}{(\Delta - \Omega_{mi})^2 + (\frac{k}{2})^2} \right) \end{aligned} \tag{3}$$

Thus, the mechanical properties were primarily determined by the intracavity photon number n_{cav} and the cavity detuning Δ . Nevertheless, the detuning Δ was undetermined owing to the thermal-optic effect that shifted the cavity resonant frequency [10]. In the current analysis, the detuning Δ was deduced from the transduction function $H(\Delta)$ because $H(\Delta)$ relies on Δ . In detail, we obtained $H(\Delta)$ from the amplitude of mechanical spectra and deduced the detuning Δ . Ultimately, the resonant frequency $\Omega_m/2\pi$ and mechanical linewidth $\gamma/2\pi$ versus Δ and n_{cav} can be obtained in the current experiment. Accordingly, the mechanical frequency and linewidth of the mechanical breathing mode (with intrinsic frequency ~ 5.741 GHz) versus the detuning Δ are displayed in Figure 6, in case of coupling with the optical odd mode at a fixed pump power $P_{in} = -0.34$ dBm. As observed from Figure 6a, the optical spring effect was dominant in case Δ was situated farther from Ω_{mi} . In contrast, a strong anti-damping effect was observed and the intrinsic mechanical dissipation γ_i was compensated in case Δ was proximate to Ω_{mi} , as indicated in Figure 6b. Furthermore, the mechanical linewidth $\gamma/2\pi$ was almost zero and the phonon lasing effect was observed [10] when the pump power increased by approximately 2 dB. Based on these experimental data, the fitted system parameters can be described as follows: intrinsic mechanical resonant frequency $\Omega_{mi}/2\pi = 5.7412$ GHz, intrinsic mechanical quality factor $Q_{mi} = 1503$ ($\gamma_i/2\pi = 3.82$ MHz), and optomechanical coupling rate $g_0/2\pi = 0.73$ MHz. In addition, the optomechanical coupling rate between another lower frequency mechanical mode and the optical odd mode was $g_1/2\pi = 0.51$ MHz.

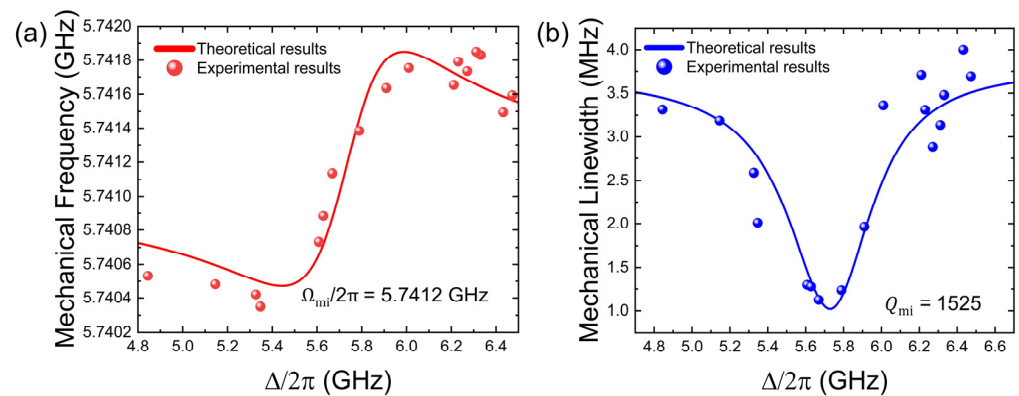


Figure 6. (a). Mechanical resonant frequency $\Omega/2\pi$ and (b). mechanical linewidth $\gamma/2\pi$ versus cavity detuning Δ for input power $P_{in} = -0.34$ dBm.

The essential parameters for the cavity were compared with the reported structures [39–42] to evaluate the performance of the proposed device, as listed in Table 1. Although the performance of the proposed device was inferior to the reported result as compared with the single-beam OMC [39], the hetero-OMC zipper cavity structure offered adequate degrees of freedom for designing multiple optical and mechanical modes. This degree of freedom is vital for the research of multimode optomechanics. For instance, the near-degenerate mechanical modes are required in the experiment of mechanical synchronization [15,16]; however, its realization for single-beam OMC is challenging. In addition, the ability to control the loss of multiple modes is essential for the investigation of non-Hermitian physics in optomechanical systems [43,44]. In context, the loss of multiple optical and mechanical modes can be independently designed based on separate heteroregions in each nanobeam. Besides, the flexibility of designing the resonant frequency of multiple optical modes by varying the gap length s enables tunable nano size optomechanical devices. As compared with the recent report of zipper cavity [40,41,45] and slot mode OMC [42], this research focuses on mechanical breathing modes with a higher resonant frequency. Thus, the average phonon occupancy of mechanical modes was lower. In addition, the high optical quality was obtained and this system functioned in the deep-sideband-resolved regime. Although the intrinsic mechanical quality factor Q_{mi} is limited by the material loss at room temperature, the material loss can be ignored at low temperature [39]. There-

fore, this structure might be available for cooling multiple mechanical oscillators into the quantum ground state and further studying the quantum multimode optomechanics.

Table 1. Comparison with various optomechanical crystal (OMC) cavities.

	Q_i	$g_0/2\pi$	$\Omega_{mi}/2\pi$	Q_{mi}
Present study Silicon hetero-OMC zipper cavity	3.9×10^5	0.73 MHz	5.7412 GHz	1.5×10^3 (Room temperature)
Ref [39] Silicon single-beam OMC	1.22×10^6	1.1 MHz	5.1 GHz	6.8×10^5 (6 K)
Ref [40] Silicon optical zipper cavity	2×10^5	–	–	–
Ref [41] Silicon OMC zipper cavity	1.14×10^5	0.725 MHz	28 MHz	1.66×10^5 (16 K)
Ref [42] Silicon nitride slot mode OMC	3.2×10^4	0.32 MHz	3.49 GHz	2.4×10^3 (Room temperature)

4. Conclusions

In this study, we proposed and designed a hetero-OMC zipper cavity for multimode optomechanics, wherein the mechanical coherence was ensured by the heterostructure and high-frequency mechanical modes. Besides, the optical quality factor and optomechanical coupling rate were simultaneously optimized by varying geometric parameters. Consequently, the optomechanical coupling rate $g = 0.73$ MHz between a mechanical breathing mode proximate to 5.741 GHz and an optical odd mode with the dissipation rate $k/2\pi = 0.538$ GHz was experimentally reported at the deep-sideband-resolved regime. The proposed hetero-OMC zipper cavity with high flexibility of design and state-of-the-art optomechanical properties offered a reliable platform for demonstrating various experiments for multimode optomechanics.

Author Contributions: Conceptualization, K.C. and N.W.; methodology, K.C. and N.W.; software, N.W.; validation, K.C., N.W. and Y.H.; formal analysis, N.W.; investigation, N.W.; resources, K.C. and Y.H.; data curation, K.C.; writing—original draft preparation, K.C. and N.W.; writing—review and editing, X.F., F.L., W.Z. and Y.H. All authors have read and agreed to the published version of the manuscript.

Funding: This research was funded by the National Key R&D Program of China (Contract No. 2018YFB2200402); National Natural Science Foundation of China (Grant No. 91750206, 61775115); Beijing Municipal Science Technology Commission Z201100004020010; Beijing National Science Foundation contract Z180012; Beijing Frontier Science Center for Quantum Information; and Beijing Academy of Quantum Information Sciences.

Institutional Review Board Statement: Not applicable.

Informed Consent Statement: Not applicable.

Data Availability Statement: The data supporting the plots along with the additional findings reported in this paper are available from the corresponding author upon reasonable request.

Acknowledgments: The authors express their gratitude to Tianjin H-Chip Technology Group Corporation, Innovation Center of Advanced Optoelectronic Chip and Institute for Electronics and Information Technology in Tianjin, Tsinghua University for their fabrication support with EBL and ICP etching.

Conflicts of Interest: The authors declare no conflict of interest.

References

1. Aspelmeyer, M.; Kippenberg, T.J.; Marquardt, F. Cavity Optomechanics. *Rev. Mod. Phys.* **2014**, *86*, 1391–1452. [[CrossRef](#)]
2. Kippenberg, T.J.; Vahala, K.J. Cavity Optomechanics: Back-Action at the Mesoscale. *Science* **2008**, *321*, 1172–1176. [[CrossRef](#)] [[PubMed](#)]
3. Chan, J.; Alegre, T.P.M.; Safavi-Naeini, A.H.; Hill, J.T.; Krause, A.; Gröblacher, S.; Aspelmeyer, M.; Painter, O. Laser Cooling of a Nanomechanical Oscillator into Its Quantum Ground State. *Nature* **2011**, *478*, 89–92. [[CrossRef](#)] [[PubMed](#)]
4. Delić, U.; Reisenbauer, M.; Dare, K.; Grass, D.; Vuletić, V.; Kiesel, N.; Aspelmeyer, M. Cooling of a Levitated Nanoparticle to the Motional Quantum Ground State. *Science* **2020**, *367*, 892–895. [[CrossRef](#)]
5. Safavi-Naeini, A.H.; Alegre, T.P.M.; Chan, J.; Eichenfield, M.; Winger, M.; Lin, Q.; Hill, J.T.; Chang, D.E.; Painter, O. Electromagnetically Induced Transparency and Slow Light with Optomechanics. *Nature* **2011**, *472*, 69–73. [[CrossRef](#)]
6. Weis, S.; Rivière, R.; Deléglise, S.; Gavartin, E.; Arcizet, O.; Schliesser, A.; Kippenberg, T.J. Optomechanically Induced Transparency. *Science* **2010**, *330*, 1520–1523. [[CrossRef](#)]
7. Gröblacher, S.; Hammerer, K.; Vanner, M.R.; Aspelmeyer, M. Observation of Strong Coupling between a Micromechanical Resonator and an Optical Cavity Field. *Nature* **2009**, *460*, 724–727. [[CrossRef](#)]
8. Verhagen, E.; Deléglise, S.; Weis, S.; Schliesser, A.; Kippenberg, T.J. Quantum-Coherent Coupling of a Mechanical Oscillator to an Optical Cavity Mode. *Nature* **2012**, *482*, 63–67. [[CrossRef](#)]
9. Krause, A.G.; Winger, M.; Blasius, T.D.; Lin, Q.; Painter, O. A High-Resolution Microchip Optomechanical Accelerometer. *Nat. Photonics* **2012**, *6*, 768–772. [[CrossRef](#)]
10. Cui, K.; Huang, Z.; Wu, N.; Xu, Q.; Pan, F.; Xiong, J.; Feng, X.; Liu, F.; Zhang, W.; Huang, Y. Phonon Lasing in a Hetero Optomechanical Crystal Cavity. *Photonics Res.* **2021**, *9*, 937. [[CrossRef](#)]
11. Pan, F.; Cui, K.; Bai, G.; Feng, X.; Liu, F.; Zhang, W.; Huang, Y. Radiation-Pressure-Antidamping Enhanced Optomechanical Spring Sensing. *ACS Photonics* **2018**, *5*, 4164–4169. [[CrossRef](#)]
12. Li, B.-B.; Bilek, J.; Hoff, U.B.; Madsen, L.S.; Forstner, S.; Prakash, V.; Schäfermeier, C.; Gehring, T.; Bowen, W.P.; Andersen, U.L. Quantum Enhanced Optomechanical Magnetometry. *Optica* **2018**, *5*, 850. [[CrossRef](#)]
13. Hill, J.T.; Safavi-Naeini, A.H.; Chan, J.; Painter, O. Coherent Optical Wavelength Conversion via Cavity Optomechanics. *Nat. Commun.* **2012**, *3*, 1196. [[CrossRef](#)] [[PubMed](#)]
14. Arnold, G.; Wulf, M.; Barzanjeh, S.; Redchenko, E.S.; Rueda, A.; Hease, W.J.; Hassani, F.; Fink, J.M. Converting Microwave and Telecom Photons with a Silicon Photonic Nanomechanical Interface. *Nat. Commun.* **2020**, *11*, 4460. [[CrossRef](#)]
15. Colombano, M.F.; Arregui, G.; Capuj, N.E.; Pitanti, A.; Maire, J.; Griol, A.; Garrido, B.; Martinez, A.; Sotomayor-Torres, C.M.; Navarro-Urrios, D. Synchronization of Optomechanical Nanobeams by Mechanical Interaction. *Phys. Rev. Lett.* **2019**, *123*, 017402. [[CrossRef](#)]
16. Zhang, M.; Wiederhecker, G.S.; Manipatruni, S.; Barnard, A.; McEuen, P.; Lipson, M. Synchronization of Micromechanical Oscillators Using Light. *Phys. Rev. Lett.* **2012**, *109*, 233906. [[CrossRef](#)]
17. Xu, H.; Mason, D.; Jiang, L.; Harris, J.G.E. Topological Energy Transfer in an Optomechanical System with Exceptional Points. *Nature* **2016**, *537*, 80–83. [[CrossRef](#)]
18. Xu, Z.; Gao, X.; Bang, J.; Jacob, Z.; Li, T. Non-Reciprocal Energy Transfer through the Casimir Effect. *Nat. Nanotechnol.* **2021**, 1–5. [[CrossRef](#)]
19. Xu, H.; Jiang, L.; Clerk, A.A.; Harris, J.G.E. Nonreciprocal Control and Cooling of Phonon Modes in an Optomechanical System. *Nature* **2019**, *568*, 65–69. [[CrossRef](#)]
20. Ockeloen-Korppi, C.F.; Damskäg, E.; Pirkkalainen, J.-M.; Asjad, M.; Clerk, A.A.; Massel, F.; Woolley, M.J.; Sillanpää, M.A. Stabilized Entanglement of Massive Mechanical Oscillators. *Nature* **2018**, *556*, 478–482. [[CrossRef](#)]
21. Lin, Q.; Rosenberg, J.; Chang, D.; Camacho, R.; Eichenfield, M.; Vahala, K.J.; Painter, O. Coherent Mixing of Mechanical Excitations in Nano-Optomechanical Structures. *Nat. Photonics* **2010**, *4*, 236–242. [[CrossRef](#)]
22. Thompson, J.D.; Zwickl, B.M.; Jayich, A.M.; Marquardt, F.; Girvin, S.M.; Harris, J.G.E. Strong Dispersive Coupling of a High-Finesse Cavity to a Micromechanical Membrane. *Nature* **2008**, *452*, 72–75. [[CrossRef](#)] [[PubMed](#)]
23. Thijssen, R.; Verhagen, E.; Kippenberg, T.J.; Polman, A. Plasmon Nanomechanical Coupling for Nanoscale Transduction. *Nano Lett.* **2013**, *13*, 3293–3297. [[CrossRef](#)] [[PubMed](#)]
24. Roxworthy, B.J.; Aksyuk, V.A. Electrically Tunable Plasmomechanical Oscillators for Localized Modulation, Transduction, and Amplification. *Optica* **2018**, *5*, 71. [[CrossRef](#)]
25. Koya, A.N.; Cunha, J.; Guerrero-Becerra, K.A.; Garoli, D.; Wang, T.; Juodkazis, S.; Proietti Zaccaria, R. Plasmomechanical Systems: Principles and Applications. *Adv. Funct. Mater.* **2021**, *31*, 2103706. [[CrossRef](#)]
26. Asano, M.; Zhang, G.; Tawara, T.; Yamaguchi, H.; Okamoto, H. Near-Field Cavity Optomechanical Coupling in a Compound Semiconductor Nanowire. *Commun. Phys.* **2020**, *3*, 230. [[CrossRef](#)]
27. MacCabe, G.S.; Ren, H.; Luo, J.; Cohen, J.D.; Zhou, H.; Sipahigil, A.; Mirhosseini, M.; Painter, O. Nano-Acoustic Resonator with Ultralong Phonon Lifetime. *Science* **2020**, *370*, 840–843. [[CrossRef](#)]
28. Huang, Z.; Cui, K.; Li, Y.; Feng, X.; Liu, F.; Zhang, W.; Huang, Y. Strong Optomechanical Coupling in Nanobeam Cavities Based on Hetero Optomechanical Crystals. *Sci. Rep.* **2015**, *5*, 15964. [[CrossRef](#)]
29. Li, Y.; Cui, K.; Feng, X.; Huang, Y.; Huang, Z.; Liu, F.; Zhang, W. Optomechanical Crystal Nanobeam Cavity with High Optomechanical Coupling Rate. *J. Opt.* **2015**, *17*, 045001. [[CrossRef](#)]

30. Safavi-Naeini, A.H.; Van Thourhout, D.; Baets, R.; Van Laer, R. Controlling Phonons and Photons at the Wavelength-Scale: Silicon Photonics Meets Silicon Phononics. *Optica* **2019**, *6*, 213. [[CrossRef](#)]
31. Qi, R.; Xu, Q.; Wu, N.; Cui, K.; Zhang, W.; Huang, Y. Nonsuspended Optomechanical Crystal Cavities Using As₂S₃ Chalcogenide Glass. *Photonics Res.* **2021**, *9*, 893. [[CrossRef](#)]
32. Xiong, H.; Wu, Y. Fundamentals and Applications of Optomechanically Induced Transparency. *Appl. Phys. Rev.* **2018**, *5*, 031305. [[CrossRef](#)]
33. Chew, X.; Zhou, G.; Chau, F.S.; Deng, J.; Tang, X.; Loke, Y.C. Dynamic Tuning of an Optical Resonator through MEMS-Driven Coupled Photonic Crystal Nanocavities. *Opt. Lett.* **2010**, *35*, 2517. [[CrossRef](#)] [[PubMed](#)]
34. Huang, Z.; Cui, K.; Bai, G.; Feng, X.; Liu, F.; Zhang, W.; Huang, Y. High-Mechanical-Frequency Characteristics of Optomechanical Crystal Cavity with Coupling Waveguide. *Sci. Rep.* **2016**, *6*, 34160. [[CrossRef](#)] [[PubMed](#)]
35. Schliesser, A.; Rivière, R.; Anetsberger, G.; Arcizet, O.; Kippenberg, T.J. Resolved-Sideband Cooling of a Micromechanical Oscillator. *Nat. Phys.* **2008**, *4*, 415–419. [[CrossRef](#)]
36. Burek, M.J.; Cohen, J.D.; Meenehan, S.M.; El-Sawah, N.; Chia, C.; Ruelle, T.; Meesala, S.; Rochman, J.; Atikian, H.A.; Markham, M.; et al. Diamond Optomechanical Crystals. *Optica* **2016**, *3*, 1404. [[CrossRef](#)]
37. Carmon, T.; Yang, L.; Vahala, K.J. Dynamical Thermal Behavior and Thermal Selfstability of Microcavities. *Opt. Express* **2004**, *12*, 9. [[CrossRef](#)]
38. Gorodetsky, M.L.; Schliesser, A.; Anetsberger, G.; Deleglise, S.; Kippenberg, T.J. Determination of the Vacuum Optomechanical Coupling Rate Using Frequency Noise Calibration. *Opt. Express* **2010**, *18*, 23236. [[CrossRef](#)]
39. Chan, J.; Safavi-Naeini, A.H.; Hill, J.T.; Meenehan, S.; Painter, O. Optimized Optomechanical Crystal Cavity with Acoustic Radiation Shield. *Appl. Phys. Lett.* **2012**, *101*, 081115. [[CrossRef](#)]
40. Deotare, P.B.; McCutcheon, M.W.; Frank, I.W.; Khan, M.; Lončar, M. Coupled Photonic Crystal Nanobeam Cavities. *Appl. Phys. Lett.* **2009**, *95*, 031102. [[CrossRef](#)]
41. Safavi-Naeini, A.H.; Gröblacher, S.; Hill, J.T.; Chan, J.; Aspelmeyer, M.; Painter, O. Squeezed Light from a Silicon Micromechanical Resonator. *Nature* **2013**, *500*, 185–189. [[CrossRef](#)] [[PubMed](#)]
42. Grutter, K.E.; Davanço, M.I.; Srinivasan, K. Slot-Mode Optomechanical Crystals: A Versatile Platform for Multimode Optomechanics. *Optica* **2015**, *2*, 994. [[CrossRef](#)] [[PubMed](#)]
43. Jing, H.; Özdemir, S.K.; Lü, X.-Y.; Zhang, J.; Yang, L.; Nori, F. PT-Symmetric Phonon Laser. *Phys. Rev. Lett.* **2014**, *113*, 053604. [[CrossRef](#)] [[PubMed](#)]
44. Zhang, J.; Peng, B.; Özdemir, S.K.; Pichler, K.; Krimer, D.O.; Zhao, G.; Nori, F.; Liu, Y.; Rotter, S.; Yang, L. A Phonon Laser Operating at an Exceptional Point. *Nat. Photonics* **2018**, *12*, 479–484. [[CrossRef](#)]
45. Qiao, Q.; Xia, J.; Lee, C.; Zhou, G. Applications of Photonic Crystal Nanobeam Cavities for Sensing. *Micromachines* **2018**, *9*, 541. [[CrossRef](#)] [[PubMed](#)]